arXiv:1512.09099v1 [cond-mat.mtrl-sci] 30 Dec 2015

Unoccupied electronic structure and signatures of topological Fermi arcs in the Weyl semimetal candidate $Mo_xW_{1-x}Te_2$

Ilya Belopolski*,[1,†] Su-Yang Xu*,[1] Yukiaki Ishida*,[2] Xingchen Pan*,[3] Peng Yu*,[4] Daniel S. Sanchez,[1] Madhab Neupane,[5] Nasser Alidoust,[1] Guoqing Chang,[6,7] Tay-Rong Chang,[8] Yun Wu,[9] Guang Bian,[1] Hao Zheng,[1] Shin-Ming Huang,[6,7] Chi-Cheng Lee,[6,7] Daixiang Mou,[9] Lunan Huang,[9] You Song,[10] Baigeng Wang,[3] Guanghou Wang,[3] Yao-Wen Yeh,[11] Nan Yao,[11] Julien Rault,[12] Patrick Lefevre,[12] François Bertran,[12] Horng-Tay Jeng,[8,13] Takeshi Kondo,[2] Adam Kaminski,[9] Hsin Lin,[6,7] Zheng Liu,[4,14,15,‡] Fengqi Song,[3,§] Shik Shin,[2] and M. Zahid Hasan[1,11,¶]

[1]*Laboratory for Topological Quantum Matter and Spectroscopy (B7), Department of Physics, Princeton University, Princeton, New Jersey 08544, USA*

[2]*The Institute for Solid State Physics (ISSP), University of Tokyo, Kashiwa-no-ha, Kashiwa, Chiba 277-8581, Japan*

[3]*National Laboratory of Solid State Microstructures, Collaborative Innovation Center of Advanced Microstructures, and Department of Physics, Nanjing University, Nanjing, 210093, P. R. China*

[4]*Centre for Programmable Materials, School of Materials Science and Engineering, Nanyang Technological University, 639798, Singapore*

[5]*Department of Physics, University of Central Florida, Orlando, FL 32816, USA*

[6]*Centre for Advanced 2D Materials and Graphene Research Centre, National University of Singapore, 6 Science Drive 2, 117546, Singapore*

[7]*Department of Physics, National University of Singapore, 2 Science Drive 3, 117546, Singapore*

[8]*Department of Physics, National Tsing Hua University, Hsinchu 30013, Taiwan*

[9]*Ames Laboratory, U.S. DOE and Department of Physics and Astronomy, Iowa State University, Ames, Iowa 50011, USA*

[10]*State Key Laboratory of Coordination Chemistry,*

* These authors contributed equally to this work.

School of Chemistry and Chemical Engineering,
Collaborative Innovation Center of Advanced Microstructures,
Nanjing University, Nanjing, 210093, P. R. China
[11]*Princeton Institute for Science and Technology of Materials,*
Princeton University, Princeton, New Jersey, 08544, USA
[12]*Synchrotron SOLEIL, L'Orme des Merisiers,*
Saint-Aubin-BP 48, 91192 Gif-sur-Yvette, France
[13]*Institute of Physics, Academia Sinica, Taipei 11529, Taiwan*
[14]*NOVITAS, Nanoelectronics Centre of Excellence,*
School of Electrical and Electronic Engineering,
Nanyang Technological University, 639798, Singapore
[15]*CINTRA CNRS/NTU/THALES, UMI 3288,*
Research Techno Plaza, 50 Nanyang Drive,
Border X Block, Level 6, 637553, Singapore

(Dated: December 31, 2015)

Abstract

Weyl semimetals have sparked intense research interest, but experimental work has been limited to the TaAs family of compounds. Recently, a number of theoretical works have predicted that compounds in the $Mo_xW_{1-x}Te_2$ series are Weyl semimetals. Such proposals are particularly exciting because $Mo_xW_{1-x}Te_2$ has a quasi two-dimensional crystal structure well-suited to many transport experiments, while WTe_2 and $MoTe_2$ have already been the subject of numerous proposals for device applications. However, with available ARPES techniques it is challenging to demonstrate a Weyl semimetal in $Mo_xW_{1-x}Te_2$. According to the predictions, the Weyl points are above the Fermi level, the system approaches two critical points as a function of doping, there are many irrelevant bulk bands, the Fermi arcs are nearly degenerate with bulk bands and the bulk band gap is small. Here, we study $Mo_xW_{1-x}Te_2$ for $x = 0.07$ and 0.45 using pump-probe ARPES. The system exhibits a dramatic response to the pump laser and we successfully access states > 0.2eV above the Fermi level. For the first time, we observe direct, experimental signatures of Fermi arcs in $Mo_xW_{1-x}Te_2$, which agree well with theoretical calculations of the surface states. However, we caution that the interpretation of these features depends sensitively on free parameters in the surface state calculation. We comment on the prospect of conclusively demonstrating a Weyl semimetal in $Mo_xW_{1-x}Te_2$.

Weyl fermions have been known since the early twentieth century as chiral particles associated with solutions to the Dirac equation at zero mass [1, 2]. Although they arise naturally in quantum field theory, they are not known to exist as fundamental particles in nature. However, Weyl fermions are closely related to accidental degeneracies in the band structures of crystals [3–10]. By taking advantage of this correspondence, Weyl fermions were observed for the first time, earlier this year, as emergent quasiparticles in the crystal TaAs and in a photonic crystal [11–15]. Such crystals, Weyl semimetals, also host an unusual topological classification that protects topological Fermi arcs on the surface of a bulk sample [7–9]. The bulk Weyl fermions and surface Fermi arcs of a Weyl semimetal are predicted to give rise to a wealth of unusual transport phenomena [16, 17]. These effects are associated both with the non-trivial topological invariants of a Weyl semimetal and with a variety of phenomena relating to Weyl fermions in quantum field theory. To explore and apply these phenomena, it is important to discover new Weyl semimetals.

Recently, several works have proposed that WTe_2, $MoTe_2$ and $Mo_xW_{1-x}Te_2$ are Weyl semimetals [18–21]. The $Mo_xW_{1-x}Te_2$ series may be desirable for transport experiments because it has a highly-layered crystal structure. Indeed, there have already been numerous device proposals for this series, including one proposal for a novel type of transistor based on laser patterning of $MoTe_2$ thin films and another proposal for a topological edge state transistor based on the quantum spin Hall effect in single-layer $MoTe_2$ [22, 23]. The intense interest in developing novel devices based on $Mo_xW_{1-x}Te_2$ suggests that this series may not only provide the first Weyl semimetal outside the TaAs family of compounds, but may also make experimentally accessible novel transport phenomena in Weyl semimetals. In addition, the emergent Weyl fermions in $Mo_xW_{1-x}Te_2$ are predicted to violate Lorentz invariance, leading to an unexpected and fascinating connection with previously ignored quantum field theories [19].

Despite the intense interest in Weyl semimetals and the unusual properties of $Mo_xW_{1-x}Te_2$, it is exceedingly challenging to experimentally demonstrate a Weyl semimetal in this series. Specifically, WTe_2 is close to a critical point for a topological phase transition. Indeed, different theoretical works have predicted that WTe_2 is a Weyl semimetal or an insulator by using lattice constants from different X-ray diffraction experiments [18, 19]. A related concern is the small separation of the Weyl points in momentum space, exceeding the available experimental resolution. Lastly, the Weyl points are above the Fermi level, mak-

ing them challenging to access using standard angle-resolved photoemission spectroscopy (ARPES). To stabilize the Weyl semimetal phase and increase the momentum-space separation of the Weyl points, it has been proposed to dope WTe_2 with Mo [18]. Further, to study the band structure above the Fermi level, it is possible to use pump-probe ARPES. Pump-probe ARPES uses twin lasers to excite electrons above the Fermi level and then perform photoelectron spectroscopy on the excited electrons, giving access to states above the Fermi level. At the same time, the low photon energy afforded by a laser maximizes momentum resolution, ideal for the study of closely-spaced features of the band structure.

Here, we study 7% and 45% Mo-doped WTe_2 using pump-probe ARPES. We successfully access states > 0.2eV above the Fermi level, well above the energies of the Weyl points [18, 19]. We find excellent agreement with *ab initio* calculations of surface states. We observe features in the data which may be Fermi arcs. However, we find that the interpretation of the features as Fermi arcs depends sensitively on free parameters in the calculation. We suggest that a careful composition dependence of the $Mo_xW_{1-x}Te_2$ series can provide more conclusive evidence of Fermi arcs, possibly demonstrating a Weyl semimetal. Our work provides the first step to observing a dramatic violation of Lorentz invariance in the band structure of a crystal.

The crystal structure of $Mo_xW_{1-x}Te_2$ with an orthorhombic Bravais lattice, space group $Pmn2_1$ (#31) and lattice constants $a = 6.282$Å, $b = 3.496$Å, and $c = 14.07$Å is shown in Fig. 1(a) [24]. The atomic structure is layered, with single layers of W/Mo sandwiched in-between Te bilayers, which are stacked along the z-axis and held together by Van der Waals interactions, see Fig. 1(a). Seen from Fig. 1(b), the W/Mo atoms are shifted away from the center of the hexagon formed by the Te atoms. This makes the in-plane lattice constant a longer than the b lattice constant. Additionally, the distance between adjacent W/Mo atoms is appreciably smaller along $\hat{x}$ than the others, creating high anisotropy. The lack of inversion symmetry is a crucial condition for the Weyl semimetal state in $Mo_xW_{1-x}Te_2$. Shown in Fig. 1(c) is the scanning electron microscope (SEM) image showing the layered structure of the crystals used in this study. Furthermore, energy-dispersive spectroscopy (EDS) measurements show that the average bulk crystals have composition $Mo_{0.45}W_{0.55}Te_2$, see Methods. The bulk and (001) surface Brillouin zone (BZ) of $Mo_xW_{1-x}Te_2$ is shown in Fig. 1(d). In Fig. 1(e), we display the bulk band structure of WTe_2 along high-symmetry directions. We find that the valence and conduction bands approach each other near Γ.

Therefore, 8 Weyl points are found on the $k_z = 0$ plane for $Mo_{0.2}W_{0.8}Te_2$, which are formed by the topmost valence and lowest conduction bands, see Fig. 1(g). In Fig. 1(f) we note the energy offset between certain Weyl points along the k_x direction. Note, the Weyl points are represented by red and white circles to signify their $+1$ or -1 chirality. As shown, two Weyl points are situated -0.08eV above E_F and two additional Weyl points at -0.08eV above E_F for $Mo_{0.2}W_{0.8}Te_2$. To convey the difference and uniqueness of the Lorentz-violating Weyl cone in $Mo_xW_{1-x}Te_2$, we compare them with the Lorentz invariant Weyl points recently discovered in the TaAs family of inversion-symmetry breaking single crystals [11–15] in the cartoon schematic shown in Fig. 1(h). The Lorentz-violating Weyl points, in contrast to the point-like Fermi surface of Lorentz invariant Weyl nodes, have an open Fermi surface. The novel Weyl points in $Mo_xW_{1-x}Te_2$ grant access to Weyl physics previously ignored in quantum field theory. To resolve the Weyl semimetal state in $Mo_{0.45}W_{0.55}Te_2$ we use vacuum ultraviolet angle-resolved photoemission spectroscopy (ARPES) and pump-probe ARPES. In Fig. 1(i,j) we show the Fermi surface by vacuum ultraviolet APRES on the (001) surface of $Mo_{0.45}W_{0.55}Te_2$ along the $\bar{Y}$-$\bar{\Gamma}$-$\bar{Y}$ direction. The Fermi surface at E_F shows a palmier shaped hole pocket and an almond shaped electron pocket adjacent to the $\bar{\Gamma}$ pocket.

We show that our ARPES spectra agree well with first principles calculations below the Fermi level. This provides an important reference point for understanding the band structure at energies above the Fermi level, where the Weyl points and Fermi arcs are predicted to exist. Figs. 2(a-c) show the constant energy contours over the k-space range defined by the green dotted box in Fig. 1(j). At the Fermi level, we observe a palmier-shaped pocket and an almond-shaped pocket, see Fig. 2(a). As one goes from the Fermi level to higher binding energies, the palmier-shaped pocket expands while the almond-shaped pocket shrinks, see Figs. 2(a-c). This shows that the palmier-shaped pocket is hole-like whereas the almond-shaped pocket is electron-like. We show the energy dispersion along two cuts, namely Cut 1 and Cut 2 defined in Fig. 2(d). In Cut 1, shown in Figs. 2(h,i), we observe an electron band and two hole bands at the Fermi level. This is consistent with the fact that Cut 1 goes through the electron pocket and the two convex parts of the hole pocket. In Cut 2, shown in Fig. 2(j), we observe only the electron band at the Fermi level whereas the hole band disperses to higher binding energies. We compare our Fermi surface with an *ab initio* calculation of the Fermi surface for $Mo_{0.2}W_{0.8}Te_2$. We find that the electron and hole pockets agree well with our experimental data, providing the clearest correspondence yet reported

between *ab initio* calculation and ARPES for $Mo_xW_{1-x}Te_2$ [25–27]. The constant energy contours in Figs. 2(k-o) show the zoomed-in view of the region of approach between the electron and hole pockets. We see that, as one goes from higher binding energies to the Fermi level, the two pockets gradually approach each other. At the Fermi level, shown in Fig. 2(k), the separation between the two pockets is small but finite. We show a series of the band dispersions in Figs. 2(p-s), where, again, we observe both the electron and the hole bands. It is important to note that the ARPES data are dominated by the contribution from surface states, or more precisely, states which are mostly localized on the surface and whose spectral weight mainly comes from the surface region. One piece of evidence is that our constant energy contour data in Figs. 2(a-c) show excellent agreement with the theoretical calculations in Figs. 2(e-g), which only considers the spectral weight from the top unit cell of a semi-infinite system. In addition, the observed bands are sharp. If the spectral weight were due to the bulk bands, we expect the contours to be filled in with intensity due to the finite k_z resolution. Lastly, we note that the sharpest states in our ARPES spectra, the almond pocket near the region where it intersects the palmier, correspond to a state heavily localized near the surface in the calculate, indicated by a heavy red region in Figs. 2(e,g). We provide an illustration of the measured Fermi surface in Fig. 2(v). According to the theoretical calculations, as one goes to energies above the Fermi level, the two pockets are expected to further approach each other. Eventually the convex region of the palmier pocket intersects the almond pocket, giving rise to Weyl nodes.

Next, we show that the almond pocket in $Mo_{0.45}W_{0.55}Te_2$ evolves into two nested electron pockets above the Fermi level. To access the unoccupied states, we use pump-probe ARPES with a 1.49eV pump laser to excite electrons into low-lying states above the Fermi level and a 5.99eV probe laser to perform photoemission [28]. We can, further, directly and precisely control the time delay between the two lasers. Here, we suppose that the pump laser arrives always at time t_0 and we study ARPES spectra at two probe times t. For $t < t_0$, the probe arrives before the pump, so we only observe occupied states, as in normal ARPES. For $t > t_0$, the probe arrives after the pump and we observe unoccupied states. We use pump probe ARPES with $t > t_0$ to understand the band structure in $Mo_xW_{1-x}Te_2$ above the Fermi level. Corresponding spectra with $t < t_0$ serve as a reference to compare with normal ARPES. We first present a cut of $Mo_{0.45}W_{0.55}Te_2$ along the $\bar{\Gamma}$-$\bar{Y}$ direction at $k_x = 0$, see Figs. 3(a,b). The sample responds beautifully to the pump laser and we observe a

dramatic evolution of the bands up to energies > 0.2eV above the Fermi level. Note that all available calculations of $Mo_xW_{1-x}Te_2$ place the Weyl points < 0.1eV above the Fermi level. In addition, the Weyl points are all predicted to be within 0.25Å^{-1} of the $\bar{\Gamma}$ point [18–21]. We see that our pump probe measurement easily accesses the relevant region of reciprocal space. We see in Fig. 3(b) that the palmier pocket closes up at ~ -0.02eV of the Fermi level. However, the almond pocket extends well above the Fermi level. In particular, we notice two branches reaching toward $\bar{\Gamma}$ and appearing to merge at ~ -0.15eV. These bands correspond to the inner and outer contours of the almond, discussed above. We also see a broader, diffuse branch of the almond pocket reach toward the $\bar{Y}$ point. We find that above E_F, the palmier closes up rapidly while the almond expands outward into a large pair of electron pockets. To better understand this evolution, we show a Fermi surface mapping of the almond pocket above E_F, see Fig. 3 (d). We see the almond pocket grows larger above E_F, again, as an electron pocket. We also find that the almond pocket evolves into two nested contours. This structure is most easily visible at $E_\text{B} = -0.1$eV in Fig. 3 (d). We reproduce this constant energy cut in Fig. 3 (h), where we also mark the two contours by blue dotted lines. From the $\bar{\Gamma}$-$\bar{Y}$ cut, we see that this pair of nested contours corresponds to the two contours which make up the almond pocket at E_F, as shown in Fig. 2 (a). Next, we study the band structure on a cut parallel to $\bar{\Gamma}$-$\bar{X}$ at $k_y \sim 0.36\text{Å}^{-1}$, see Figs. 3(e,f). Again we see a pair of electron bands which we associate with the almond pocket. The lower branch, marked (1) in Fig. 3(g), corresponds to the sharp, prominent branch of the almond as it appears below E_F. On the other hand, the upper branch, (2) of the almond pocket has a minimum at ~ -0.02eV on this cut and is entirely above the Fermi level. In addition, we note that this upper branch appears to have a discontinuity at $k_x \sim 0.02\text{Å}^{-1}$ where it seems to break into two disjoint bands, (2) and (3). It is this feature which is our candidate Fermi arc and which we analyze at greater length below. For reference, in Fig. 3 (i) we label the cuts shown in Figs. 3 (a,b,e,f).

Next, we show that the disjoint band we observe agrees well with a topological Fermi arc found by first principles calculation. We consider a cut of $Mo_{0.45}W_{0.55}Te_2$, shown in Fig. 4(a) at $k_y = 0.325\text{Å}^{-1}$, with *ab initio* calculations taken at $k_y = k_{\text{W1}} = 0.215\text{Å}^{-1}$, Fig. 4(b-e). We note that the k_y values differ, but both correspond to the edge of the electron pocket at the Fermi level, the approximate location of the Weyl points. In addition, as we show below, the band structure features we discuss here appear robust as a function of doping.

As noted above, the discrepancy may be due to an error in determining $\bar{\Gamma}$ in experiment, an error in the approximation used for calculating doped band structures, or, especially, a systematic error due to comparing a calculation of 20% doping with a measurement of 45% doping. We further show calculations for different on-site surface potentials, 0eV and -0.11eV, in Fig. 4(b,c), respectively. We find that the two surface potentials give rise to a different connectivity pattern of the Fermi arcs [18]. In particular, for 0eV, we find that two short arcs connect neighboring Weyl points, as shown in Fig. 4(d,j), while for -0.11eV, one arc connects the two W_1 and a long arc emanates from the W_2, as shown in Fig. 4(e,k). The surface potential is difficult to predict, but can be fixed by comparison with ARPES data. Comparing our ARPES spectrum of $Mo_{0.45}W_{0.55}Te_2$ with the numerics, we see that our ARPES spectrum suggests that the two W_1 are connected by a Fermi arc, favoring the scenario in Fig. 4(k). This suggests that we have observed Fermi arcs. We also find that the energy separation of the arc features is ~ 0.03eV, consistent with the energy separation of the Weyl points. Similarly, we can estimate the momentum separation between the two arc features to be $\sim 0.03\text{Å}^{-1}$, consistent with *ab initio* calculation [18]. However, the interpretation of the features in the data is complicated by the trivial surface states. First, while the -0.11eV calculation shows two trivial electron pockets in addition to the Fermi arc, in our ARPES data we only observe in total two electron pockets. Furthermore, the 0eV calculation shows trivial surface states which agree well with the flat trivial surface state at ~ -0.1eV that merges into the bulk, giving rise to a trivial surface state arc, see Fig. 4(b). This cut further shows a trivial surface state electron pocket with branches which merge into the bulk near the flat surface state. These features also match well with the ARPES spectrum, but suggest that we see only trivial surface states. Moreover, in this case, the Fermi arcs would be nearly degenerate with adjacent trivial surface states, making them very difficult to observe given the typical linewidth of our spectra. We further study a cut of $Mo_{0.07}W_{0.93}Te_2$ at $k_y = 0.29\text{Å}^{-1}$. For these spectra, we find that p polarization selects the Fermi arc feature, see Fig. 4(f), while the s polarization gives two electron pockets, see Fig. 4(g). This suggests a total of three electron bands, which matches the -0.11eV case. However, again we can also interpret the bands as trivial pockets which appear as arcs because they merge into the bulk. Lastly, we also note that the center arc, labelled (2) in Fig. 4(i) is above the outer arcs (1) in $Mo_{0.07}W_{0.93}Te_2$, while arc (3) is below arc (2) in Fig. 2(g). This evolution of the structure as a function of composition provides one route to

clarify whether or not the disjoint feature we observe in $Mo_{0.45}W_{0.55}Te_2$ and $Mo_{0.07}W_{0.93}Te_2$ is a topological Fermi arc. By comparing our experimental data with *ab initio* calculation, we find that the disjoint band we observe in our ARPES spectra agrees with topological Fermi arcs in numerics, providing the first direct experimental signature of a topological Fermi arc in $Mo_{0.45}W_{0.55}Te_2$ and $Mo_{0.07}W_{0.93}Te_2$.

We discuss the extent to which the signatures of Fermi arcs observed here are robust. In support of an observation of Fermi arcs: (1) we observe surface states that are disjoint in their dispersion; (2) the energy spacing between the terminations of disjoint surface states also agrees with the energy difference between the W1 and W2 Weyl nodes in calculations; (3) the momentum separation of the disjoint surface state agrees within error with the separation of the Weyl nodes in calculation; (4) the overall experimentally-measured dispersions match with the calculations. However, it is important to note that, in general, a qualitative agreement between the experimental data and the theoretical calculations is not a conclusive demonstration of the Weyl semimetal state. In particular, we see that the calculated dispersion changes dramatically as a function of the on-site potential, see again Figs. 4**b,c**. As importantly, the disjoint nature of the surface states is a necessary, but not sufficient condition for showing Fermi arcs. We see that in the calculation there are trivial surface states that are not Fermi arcs but also show a disjoint dispersion. This is not surprising since a trivial state may merge into a bulk band, forming a trivial arc. This effect is particularly relevant for $Mo_xW_{1-x}Te_2$ because there are many irrelevant bulk bands at the energies of the Weyl points.

We compare the experimental results here with those in the TaAs class to further elaborate on the prospect of conclusively demonstrating Fermi arcs in $Mo_xW_{1-x}Te_2$. We have experimentally demonstrated the existence of Fermi arcs in TaAs and TaP by counting the net number of chiral surface states along a k-space loop that encloses a projected Weyl node. There, the demonstration did not rely directly on theoretical calculations and was robust. The following properties were important for achieving this robust proof in TaAs and TaP [13, 29, 30]: (1) The k-space separation between the W2 Weyl nodes in TaAs and TaP is sufficiently large, $\Delta k \sim 0.08\text{Å}^{-1}$. (2) Compared to $Mo_xW_{1-x}Te_2$, TaAs and TaP are nearly ideal semimetals, with only small irrelevant bulk bands at the energies of the Weyl nodes. Also, the bulk band structure including both the Weyl cones and the trivial bands were experimentally determined by soft X-ray ARPES. Combining these two conditions, it was

possible to find a k-space loop that encloses a projected Weyl node, and, at the same time, along which the bulk band structure has a full energy gap. Now, we evaluate the situation in $Mo_xW_{1-x}Te_2$ also based on these two conditions. (1) The k-space separation between the Weyl nodes is predicted to be $\sim 0.04\text{Å}^{-1}$ for $Mo_{0.45}W_{0.55}Te_2$ [18]. This separation, although smaller than the separation of Weyl points in TaAs, is still within the momentum resolution of ARPES. (2) $Mo_xW_{1-x}Te_2$ is highly metallic, with many irrelevant bulk bands. Moreover, the energy gap between the two bands that cross to form the Weyl nodes is small. For example, the band gap is < 15 meV at all k points along the cut connecting adjacent W_1 and W_2 [18]. For these reasons, it is difficult to demonstrate the Fermi arcs in $Mo_xW_{1-x}Te_2$ by a direct measurement of a non-zero Chern number, as can be carried out in TaAs and TaP. To conclusively demonstrate a Weyl semimetal in $Mo_xW_{1-x}Te_2$ it is necessary, instead, to observe an isolated disjoint contour. We propose to study the evolution of the candidate Fermi arc with composition, x. A switch in the connectivity at a special composition or a composition where the Fermi arc feature is well-isolated from irrelevant bands may provide a conclusive proof that $Mo_xW_{1-x}Te_2$ is a Weyl semimetal.

Methods

Synchrotron-based ARPES measurements were performed at the CASSIOPEE beamline at Soleil in Saint-Aubin, France and the I05 beamline at the Diamond Light Source (DLS) in Didcot, United Kindom. ARPES measurements were also carried out using a home-built laser-based ARPES setup at the Ames Laboratory in Ames, Iowa, United States. All measurements were conducted under ultra-high vacuum and at temperatures $\leq$ 10K. The angular and energy resolution of the synchrotron-based ARPES measurements was better than 0.2° and 20 meV, respectively. Photon energies from 15 eV to 100 eV were used. The angular and energy resolution of the home-built laser-based ARPES measurements was better than 0.1° and 5 meV, respectively. Photon energies from 5.77 eV to 6.67 eV were used.

The pump-probe ARPES apparatus consisted of a hemispherical analyzer and a mode-locked Ti:Sapphire laser system that delivered 1.48 eV pump and 5.92 eV probe pulses at a 250kHz repetition [28]. The time and energy resolution was 300 fs and 27 meV, respectively. The spot diameter of the pump and probe beams at the sample position was 250 and

85μm, respectively. Samples were cleaved in the spectrometer at $< 5 \times 10^{-11}$ Torr, and measurements were conducted at ~ 8 K.

High quality ribbon-like single crystals of $Mo_xW_{1-x}Te_2$ were grown by chemical vapor transport (CVT) with iodine (I) as the agent. Before growing the crystals, the quartz tubes were thoroughly cleaned using thermal and ultrasonic cleaning treatments to avoid contamination. Stoichiometric amounts of W (99.9% powder, Sigma-Aldrich), Mo (99.95% powder, Sigma-Aldrich) and Te (99.95%, Sigma-Aldrich) were mixed with iodine, were sealed in a 20 cm long quartz tube under vacuum $\sim 10^{?6}$ Torr, and then placed in a three-zone furnace. The reaction zone dwelled at 850 °C for 40 hours with the growth zone at 900 °C and then heated to 1070 °C for seven days with the growth zone at 950 °C. Lastly, the furnace was allowed to cool naturally down to room temperatures. The $Mo_xW_{1-x}Te_2$ single crystals were collected from the growth zone. Excess iodine adhering to the single crystals was removed by using acetone or ethanol. Nominal compositions of the $Mo_xW_{1-x}Te_2$ crystals were $x = 0.0, 0.1, 0.15, 0.2, 0.3$. An energy dispersive spectroscopy (EDS) measurement was carried out to precisely determine the composition of the samples. Samples were first surveyed by an FEI Quanta 200FEG environmental scanning electron microscope (SEM). The chemical compositions of the samples were characterized by an Oxford X-Max energy dispersive spectrometer that was attached to the SEM. All the samples were loaded at once in the SEM chamber to ensure a uniform characterization condition. Both the SEM imaging and EDS characterization were carried out at an electron acceleration voltage of 10 kV with a beam current of 0.5 nA. For each sample, three different spatial positions were randomly picked to check the uniformity. The measured compositions were: $MoTe_2$ for $x = 0$, $Mo_{0.42}W_{0.58}Te_2$ for $x = 0.1$, $Mo_{0.46}W_{0.54}Te_2$ for $x = 0.15$, $Mo_{0.44}W_{0.56}Te_2$ for $x = 0.2$ and $Mo_{0.43}W_{0.57}Te_2$ for $x = 0.3$. For $x \neq 0$, we considered the samples to all have the approximate composition $Mo_{0.45}W_{0.55}Te_2$. Single crystals of $Mo_{0.07}W_{0.93}Te_2$ were grown by the self-flux technique. Raw materials in the molar ratio of 7 : 93 : 200 = Mo : W : Te were sealed in a quartz tube under vacuum. The mixture was heated to 750 °C, held for 1 day, and then quenched in cold water. The obtained $Mo_xW_{1-x}Te_2$ powder (150 mg) and 20 g Te were placed in a new quartz tube and sealed under vacuum. The tube was heated to 900 °C, held for 1 day and then cooled down to 500 °C over 10 days. At 500 °C, the Te flux was separated by centrifugation. The crystal structure was determined by a Bruker SMART diffractometer as previously reported in Ref. [33]. Electrical transport measurements were

carried out in a homemade system with a minimum temperature of 2 K and a maximum field of 9 Tesla. Ohmic contacts were made using gold wires and silver paste. The observations of Shubnikov de haas quantum oscillations and large magnetoresistance indicated the high quality of the samples.

We computed the electronic structures by using the projector augmented wave method [34, 35] as implemented in the VASP [36–39] package within the generalized gradient approximation (GGA) schemes [39]. For WTe_2, the experimental lattice constants used were from [24]. A $8 \times 16 \times 4$ Monkhorst Pack k-point mesh was used in the computations. The lattice constants and atomic positions of $MoTe_2$ were fully optimized in a self-consistent calculation for an orthorhombic crystal structure until the force became less than 0.001 eV/Å. Spin-orbit coupling was included in our calculations. To calculate the bulk and surface electronic structures, we constructed a first-principles tight-binding model Hamiltonian for both WTe_2 and $MoTe_2$, where the tight-binding model matrix elements were calculated by projecting onto the Wannier orbitals [40–42], which used the VASP2WANNIER90 interface [43]. We used the s- and d-orbitals for W(Mo) and the p-orbitals for Te to construct Wannier functions, without performing the procedure for maximizing localization. The electronic structure of $Mo_xW_{1-x}Te_2$ samples was calculated by a linear interpolation of the tight-binding model matrix elements of WTe_2 and $MoTe_2$. The surface states were calculated by the surface Green's function technique [44], which computed the spectral weight near the surface of a semi-infinite system.

Acknowledgements

I.B. and D.S. thank Moritz Hoesch and Timur Kim for support during synchrotron ARPES measurements at Beamline I05 of Diamond Lightsource in Didcot, UK. I.B. acknowledges the support of the US National Science Foundation GRFP. X.C.P., Y.S., B.G.W., G.H.W and F.Q.S. thank the National Key Projects for Basic Research of China (Grant Nos. 2013CB922100, 2011CB922103), the National Natural Science Foundation of China (Grant Nos. 91421109, 11522432, and 21571097) and the NSF of Jiangsu province (No. BK20130054).

† Electronic address: ilyab@princeton.edu

‡ Electronic address: z.liu@ntu.edu.sg

§ Electronic address: songfengqi@nju.edu.cn

¶ Electronic address: mzhasan@princeton.edu

[1] H. Weyl. Elektron und Gravitation. Z. Phys. **56** 330 (1929).

[2] M. Peskin & D. Schroeder. *An Introduction to Quantum Field Theory* (Perseus Books, Reading, MA, 1995)

[3] C. Herring. Accidental degeneracy in the energy bands of crystals. Phys. Rev. **52** 365 (1937).

[4] A. A. Abrikosov & S. D. Beneslavskii. Some properties of gapless semiconductors of the second kind. Journal of Low Temperature Physics **5** 141 (1971).

[5] H. B. Nielsen & M. Ninomiya. The Adler-Bell-Jackiw anomaly and Weyl fermions in a crystal. *Phys. Lett. B* **130** 389 (1983).

[6] G. E. Volovik, *The Universe in a Helium Droplet* (Clarendon Press, Oxford, 2003).

[7] S. Murakami. Phase transition between the quantum spin Hall and insulator phases in 3D: emergence of a topological gapless phase. New Journal of Physics **9**, 356 (2007).

[8] A. A. Burkov & L. Balents. Weyl semimetal in a topological insulator multilayer. Phys. Rev. Lett. **107**, 127205 (2011).

[9] X. Wan *et al.* Topological semimetal and Fermi-arc surface states in the electronic structure of pyrochlore iridates. Phys. Rev. B **83**, 205101 (2011).

[10] A. Turner and A. Vishwanath. Beyond band insulators: topology of semi-metals and interacting phases. arXiv:1301.0330.

[11] S.-M. Huang *et al.* A Weyl Fermion semimetal with surface Fermi arcs in the transition metal monopnictide TaAs class. Nat. Commun. **6**, 7373 (2015).

[12] H. Weng *et al.* Weyl semimetal phase in noncentrosymmetric transition-metal monophosphides. Phys. Rev. X **5**, 011029 (2015).

[13] S.-Y. Xu *et al.* Discovery of a Weyl fermion semimetal and topological Fermi arcs. Science **349**, 613 (2015).

[14] L. Lu *et al.* Experimental observation of Weyl points. Science **349**, 622 (2015).

[15] B. Q. Lv *et al.* Experimental discovery of Weyl semimetal TaAs. Phys. Rev. X **5**, 031013

(2015).

[16] P. Hosur & X. Qi. Recent developments in transport phenomena in Weyl semimetals. Comp. Rend. Phy. **14**, 857 (2013).

[17] A. C. Potter, I. Kimchi & A. Vishwanath. Quantum oscillations from surface Fermi arcs in Weyl and Dirac semimetals. Nat. Commun. **5**, 5161 (2014).

[18] T.-R. Chang *et al.* Arc-tunable Weyl fermion metallic state in $Mo_xW_{1-x}Te_2$. arXiv:1508.06723.

[19] A. Soluyanov *et al.* Type II Weyl semimetals. Nature **527**, 495 (2015).

[20] Y. Sun *et al.* Prediction of the Weyl semimetal in orthorhombic $MoTe_2$. arXiv:1508.03501v2.

[21] Z. J. Wang *et al.* $MoTe_2$: Weyl and line node topological metal. arXiv:1511.07440v1.

[22] X. F. Qian *et al.* Quantum spin Hall effect in two-dimensional transition metal dichalcogenides. Science **346**, 1344 (2014).

[23] S. Cho *et al.* Phase patterning for ohmic homojunction contact in $MoTe_2$. Science **349**, 625 (2015).

[24] B. E. Brown. The crystal structures of WTe_2 and high-temperature $MoTe_2$. Acta. Cryst. **20** 268 (1966).

[25] Y. Wu *et al.* Temperature-induced Lifshitz transition in WTe_2. Phys. Rev. Lett. **115**, 166602 (2015).

[26] J. Jiang *et al.* Signature of strong spin-orbital coupling in the large nonsaturating magnetoresistance material WTe_2. Phys. Rev. Lett. **115**, 166601 (2015)

[27] I. Pletikosić *et al.* Electronic structure basis for the extraordinary magnetoresistance in WTe_2. Phys. Rev. Lett. **113**, 216601 (2014).

[28] Y. Ishida *et al.* Time-resolved photoemission apparatus achieving sub-20-meV energy resolution and high stability. Rev. Sci. Instr. **85**, 123904 (2014).

[29] S.-Y. Xu *et al.* Experimental discovery of a topological Weyl semimetal state in TaP. Sci. Adv. **1**, 10 (2015).

[30] I. Belopolski *et al.* Observation of surface states derived from topological Fermi arcs in the Weyl semimetal NbP. arXiv:1509.07465.

[31] Y. P. Qi *et al.* Superconductivity in Weyl semimetal candidate $MoTe_2$. arXiv:1508.03502.

[32] R. Jiang *et al.* Tunable vacuum ultraviolet laser based spectrometer for angle-resolved photoemission spectroscopy. Rev. Sci. Instr. **85**, 033902 (2014).

[33] X. C. Pan *et al.* Pressure-driven dome-shaped superconductivity and electronic structural

evolution in tungsten ditelluride. Nat. Commun. **6**, 7805 (2015).

[34] P. E. Blöchl. Projector augmented-wave method. Phys. Rev. B. **50**, 17953 (1994).

[35] G. Kresse & J. Joubert. From ultrasoft pseudopotentials to the projector augmented-wave method. Phys. Rev. B. **59**, 1758 (1999).

[36] G. Kresse & J. Hafner. *Ab initio* molecular dynamics for open-shell transition metals. Phys. Rev. B. **48**, 13115 (1993).

[37] G. Kresse & J. Furthmüller. Efficiency of *ab initio* total energy calculations for metals and semiconductors using a plane-wave basis set. Comput. Mater. Sci. **6**, 15 (1996).

[38] G. Kresse & J. Furthmüller. Efficient iterative schemes for *ab initio* total energy calculations using a plane-wave basis set. Phys. Rev. B. **54**, 11169 (1996).

[39] J. P. Perdew, K. Burke & M. Ernzerhof. Generalized gradient approximation made simple. Phys. Rev. Lett. **77**, 3865 (1996).

[40] N. Marzari & D. Vanderbilt. Maximally localized generalized Wannier functions for composite energy bands. Phys. Rev. B **56**, 12847 (1997).

[41] I. Souza, N. Marzari & D.Vanderbilt. Maximally localized Wannier functions for entangled energy bands. Phys. Rev. B **65**, 035109 (2001).

[42] A. A. Mostofi *et al.* Wannier90: a tool for obtaining maximally-localized Wannier functions. Comp. Phys. Commun. **178**, 685 (2008).

[43] C. Franchini *et al.* Maximally localized Wannier functions in $LaMnO_3$ within PBE+U, hybrid functionals and partially self-consistent GW: an efficient route to construct *ab initio* tight-binding parameters for e_g perovskites. J. Phys. Cond. Mat. **24**, 235602 (2012).

[44] H. J. Zhang *et al.* Topological insulators in Bi_2Se_3, Bi_2Te_3 and Sb_2Te_3 with a single Dirac cone on the surface. Nat. Phys. **5**, 438 (2009).

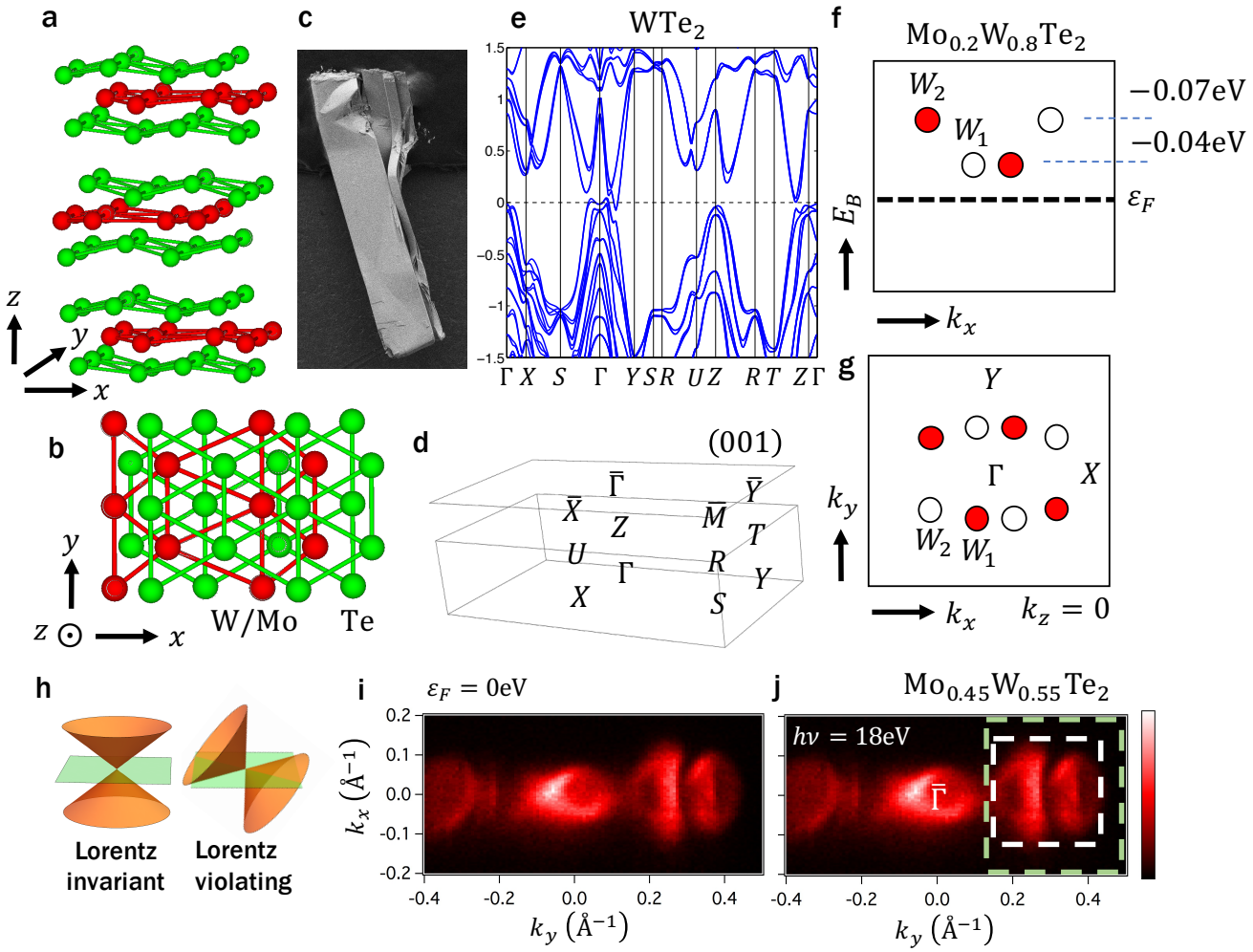
a
c
e
WTe2
f
Mo0.2W0.8Te2
W2
W1
−0.07eV
−0.04eV
εF
EB
kx
z
y
x
b
W/Mo
Te
d
(001)
Γ̄
X̄
Z
Ȳ
M̄
T
U
Γ
R
Y
X
S
g
Y
Γ
X
W2
W1
ky
kx
kz = 0
Γ X S Γ YSR UZ RT ZΓ
h
Lorentz invariant
Lorentz violating
i
εF = 0eV
kx (Å−1)
ky (Å−1)
j
Mo0.45W0.55Te2
hν = 18eV
Γ̄

FIG. 1: **Overview of $\mathbf{Mo_xW_{1-x}Te_2}$.** **a,** Side view of the $Mo_xW_{1-x}Te_2$ crystal structure. $Mo_xW_{1-x}Te_2$ crystallizes in a orthorhombic structure with space group $Pmn2_1$ (#31). The W/Mo atom layers are shown in red and the Te atom layers in green. **b,** Top view of (a), showing only one monolayer, consisting of a layer of of W/Mo atoms sandwiched between two layers of Te atoms. The structure lacks inversion symmetry. **c,** A beautiful scanning electron microscope (SEM) image of a $\sim 0.4 \times 2$ mm rectangular shaped $Mo_{0.45}W_{0.55}Te_2$ bulk crystal clearly demonstrates a layered structure. **d,** The bulk and (001) surface Brillouin zone (BZ) of $Mo_xW_{1-x}Te_2$ with high symmetry points labeled. **e,** The electronic bulk band structure of WTe_2. There is a band crossing near Γ which gives rise to electron and hole pocket along the Γ-Y direction. **f, g,** According to calculation, $Mo_{0.2}W_{0.8}Te_2$ has two sets of Weyl points, W_1 and W_2, at different energies. In total, there are eight Weyl points, all on the $k_z = 0$ plane. The red and white circles represent Weyl points with $+1$ or -1 chirality. **h,** Lorentz-invariant and Lorentz violating Weyl cones. Unlike Lorentz invariant Weyl cones, Lorentz-violating Weyl cones are tilted over, and have a constant energy contour with an electron and hole pocket touching at a point. **i, j,** Fermi surface by vacuum ultraviolet APRES on the (001) surface of $Mo_{0.45}W_{0.55}Te_2$ at $\varepsilon_F = 0$eV with an incident photon energy of 18 eV. Adjacent to the $\bar{\Gamma}$ pocket we observe a palmier-shaped hole pocket and an almond-shaped electron pocket along the $\bar{Y}$-$\bar{\Gamma}$-$\bar{Y}$ direction. The region enclosed by green dashed box corresponds to Fig. 2 (a)-(d), and that surrounded by the white dashed box corresponds to Fig. 2 (k)-(o). We expect to see Weyl points and Fermi arcs above the Fermi level in the region where the electron and hole pockets intersect.

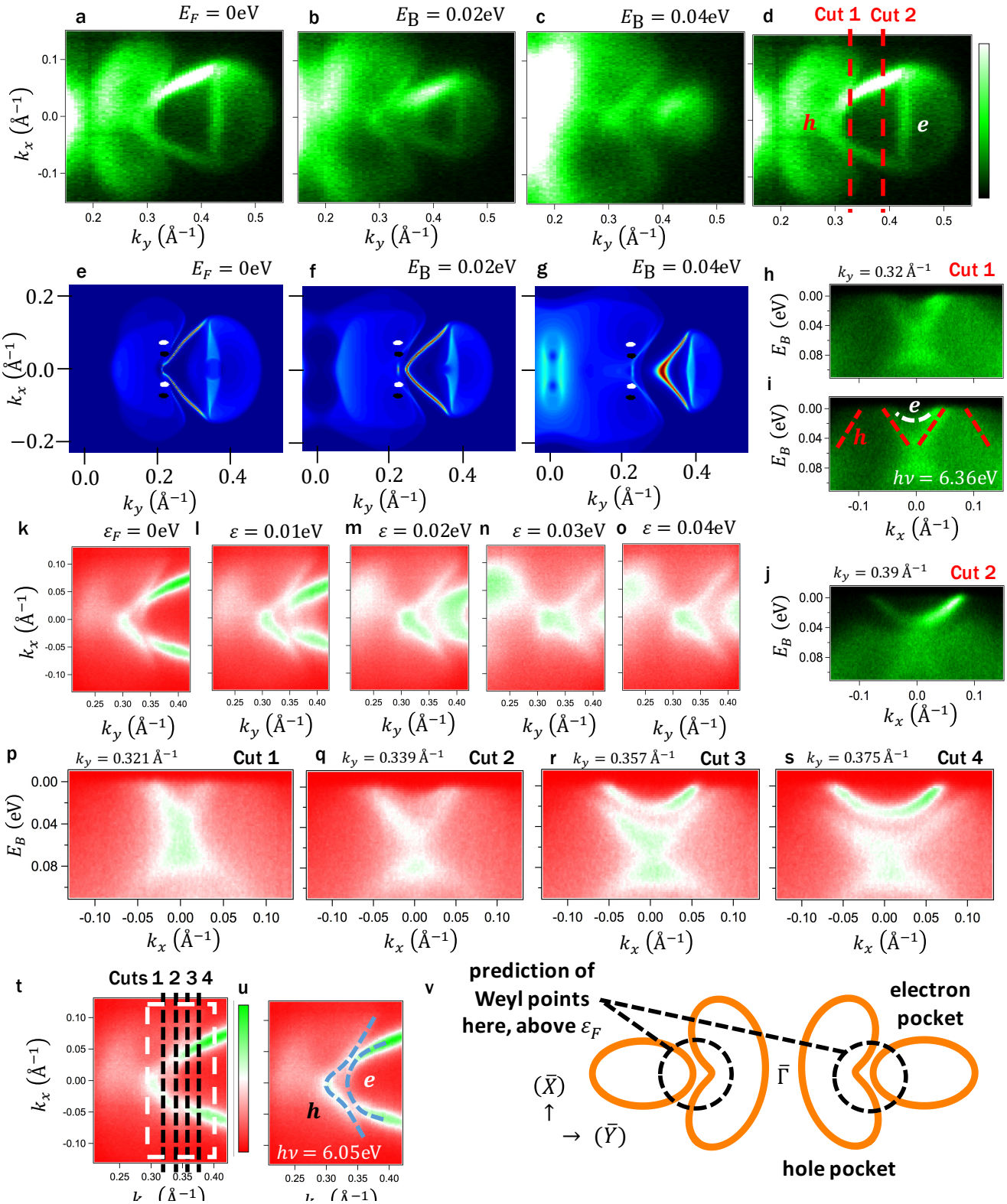
a
$E_F = 0$eV
b
$E_B = 0.02$eV
c
$E_B = 0.04$eV
d
Cut 1
Cut 2
h
e
k_x (Å^{-1})
k_y (Å^{-1})
e
$E_F = 0$eV
f
$E_B = 0.02$eV
g
$E_B = 0.04$eV
h
$k_y = 0.32$ Å^{-1}
Cut 1
i
E_B (eV)
$h\nu = 6.36$eV
k
$\varepsilon_F = 0$eV
l
$\varepsilon = 0.01$eV
m
$\varepsilon = 0.02$eV
n
$\varepsilon = 0.03$eV
o
$\varepsilon = 0.04$eV
j
$k_y = 0.39$ Å^{-1}
Cut 2
p
$k_y = 0.321$ Å^{-1}
Cut 1
q
$k_y = 0.339$ Å^{-1}
Cut 2
r
$k_y = 0.357$ Å^{-1}
Cut 3
s
$k_y = 0.375$ Å^{-1}
Cut 4
t
Cuts 1 2 3 4
u
$h\nu = 6.05$eV
v
prediction of
Weyl points
here, above ε_F
electron
pocket
hole pocket
$\bar{\Gamma}$
$(\bar{X})$
$(\bar{Y})$

FIG. 2: **$Mo_xW_{1-x}Te_2$ below the Fermi level. a-c,** ARPES measured constant energy contour maps at different binding energies using the photon energy $h\nu = 6.36$ eV. The k-space range of the maps is defined by the green dotted box in Fig. 1j. We identify a palmier-shaped hole-like pocket and an almond-shaped electron pocket. **d,** The same data as panel (a). The electron and hole pockets are labeled by e and h, respectively. **e-g,** First-principles calculated constant energy contours at different binding energies. **h,** ARPES measured $E_B - k_y$ dispersion map along Cut 1. **i,** The same data as panel (h). The dotted lines are guides to the eye that roughly trace the dispersion of the bands. **j,** ARPES measured energy dispersion map along Cut 2. Cut 1 and Cut 2 are defined by the red lines in panel (d). **k-o,** ARPES measured constant energy contour maps at different binding energies using the photon energy $h\nu = 6.05$ eV. The k-space range of the maps is defined by the white dotted box in Fig. 1j. **p-s,** ARPES measured $E_B - k_y$ dispersion maps along the cuts that are defined by the black dotted lines in panel (t). **t,u,** The same data as panel (p). The blue dotted lines in panel (u) are guides to the eye that roughly trace the electron and hole pockets at the Fermi level. **v,** Schematic illustration of the measured Fermi surface. As one goes to energies above the Fermi level, the electron and hole pockets are expected to further approach each other. Eventually the convex parts of the palmier-shaped hole pocket will touch the electron pocket, forming Weyl nodes. The dotted circles show the k-space region, in which the Weyl nodes are expected.

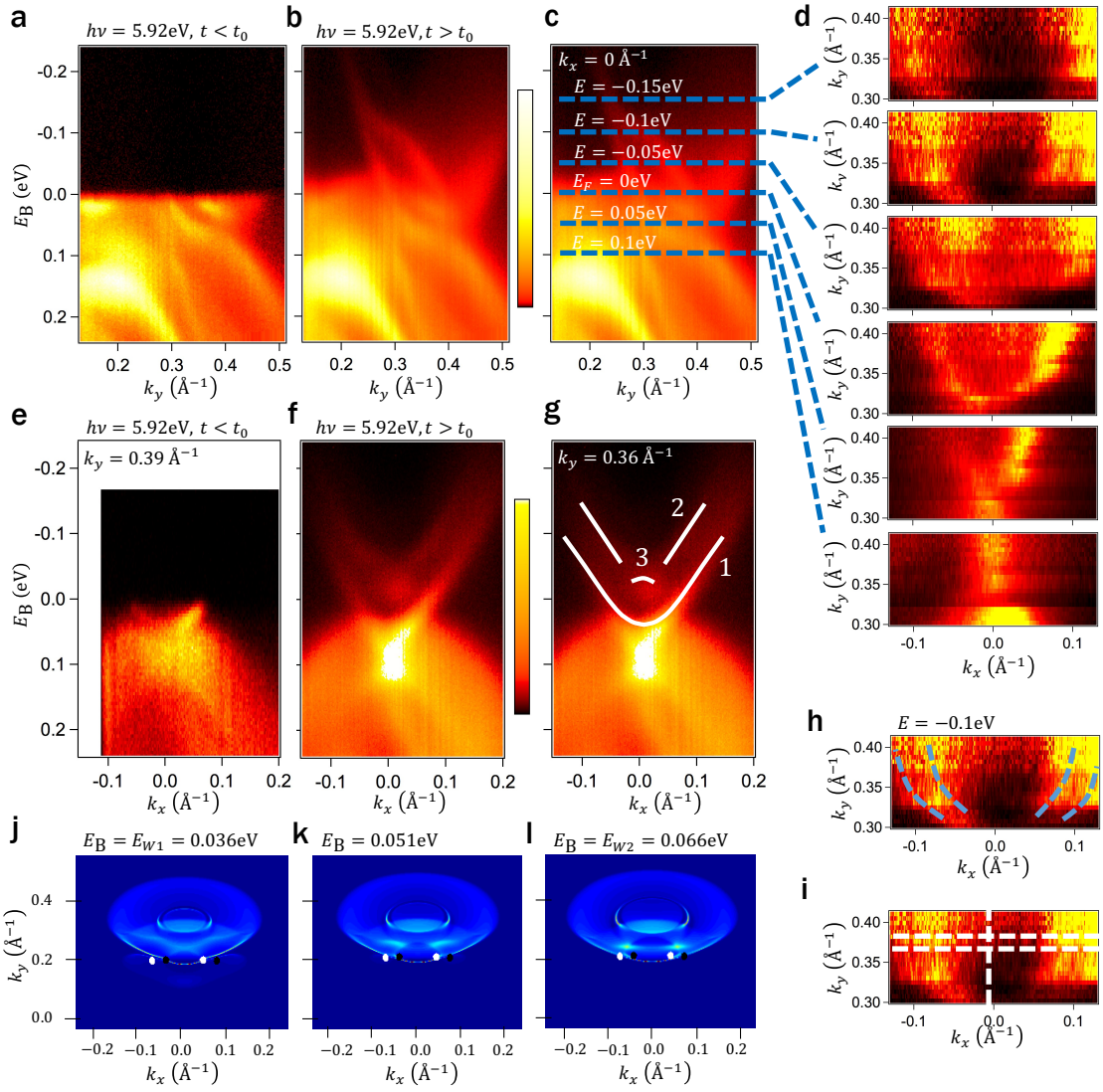
a
$h\nu = 5.92$eV, $t < t_0$
b
$h\nu = 5.92$eV, $t > t_0$
c
$k_x = 0$ Å^{-1}
$E = -0.15$eV
$E = -0.1$eV
$E = -0.05$eV
$E_F = 0$eV
$E = 0.05$eV
$E = 0.1$eV
d
E_B (eV)
k_y (Å^{-1})
k_x (Å^{-1})
e
$h\nu = 5.92$eV, $t < t_0$
$k_y = 0.39$ Å^{-1}
f
$h\nu = 5.92$eV, $t > t_0$
g
$k_y = 0.36$ Å^{-1}
1
2
3
h
$E = -0.1$eV
i
j
$E_B = E_{W1} = 0.036$eV
k
$E_B = 0.051$eV
l
$E_B = E_{W2} = 0.066$eV

FIG. 3: **$Mo_xW_{1-x}Te_2$ above the Fermi level. a, b,** We first present an energy dispersion cut of $Mo_{0.45}W_{0.55}Te_2$ along the $\bar{\Gamma}$-$\bar{Y}$ direction at $k_x = 0$. For $t < t_0$, the probe arrives before the pump, so we see only states below the Fermi level, while for $t > t_0$ the probe arrives after the pump and we observe states above the Fermi level. We see > 0.2eV above E_F, well above the energies of the Weyl points. **c,** Same as (b) but with blue dotted lines at various energies. **d,** The evolution of the Fermi surface for the almond pocket at the energy levels marked in (c). Here we observe that the almond pocket evolves into two nested contours, seen most clearly at $E_B = -0.1$eV. **e, f,** Energy dispersion of $Mo_{0.45}W_{0.55}Te_2$ for $t > t_0$ and $t < t_0$ on a cut parallel to $\bar{\Gamma}$-$\bar{X}$ at $k_y \sim 0.36$Å. For $t < t_0$ we see a single electron band, associated with the almond pocket. For $t < t_0$, we find an additional electron band with minimum at ~ -0.02eV. We observe a discontinuity in the band at $\sim \pm 0.02$Å^{-1}. **g,** Same as (f), with guides to the eye to highlight the discontinuity in the electron pocket above the Fermi level. The candidate Fermi arcs are features (2) and (3). **h,** At $E_B = -0.1$eV, the two nested contours are marked by blue dotted lines. **i,** Cuts shown in (a), (b), (e), and (f) are labeled for reference. **j-l,** Calculation of the Fermi surface for $Mo_{0.2}W_{0.8}Te_2$ above E_F. We see an electron pocket, consistent with the measured Fermi surface above E_F, (d).

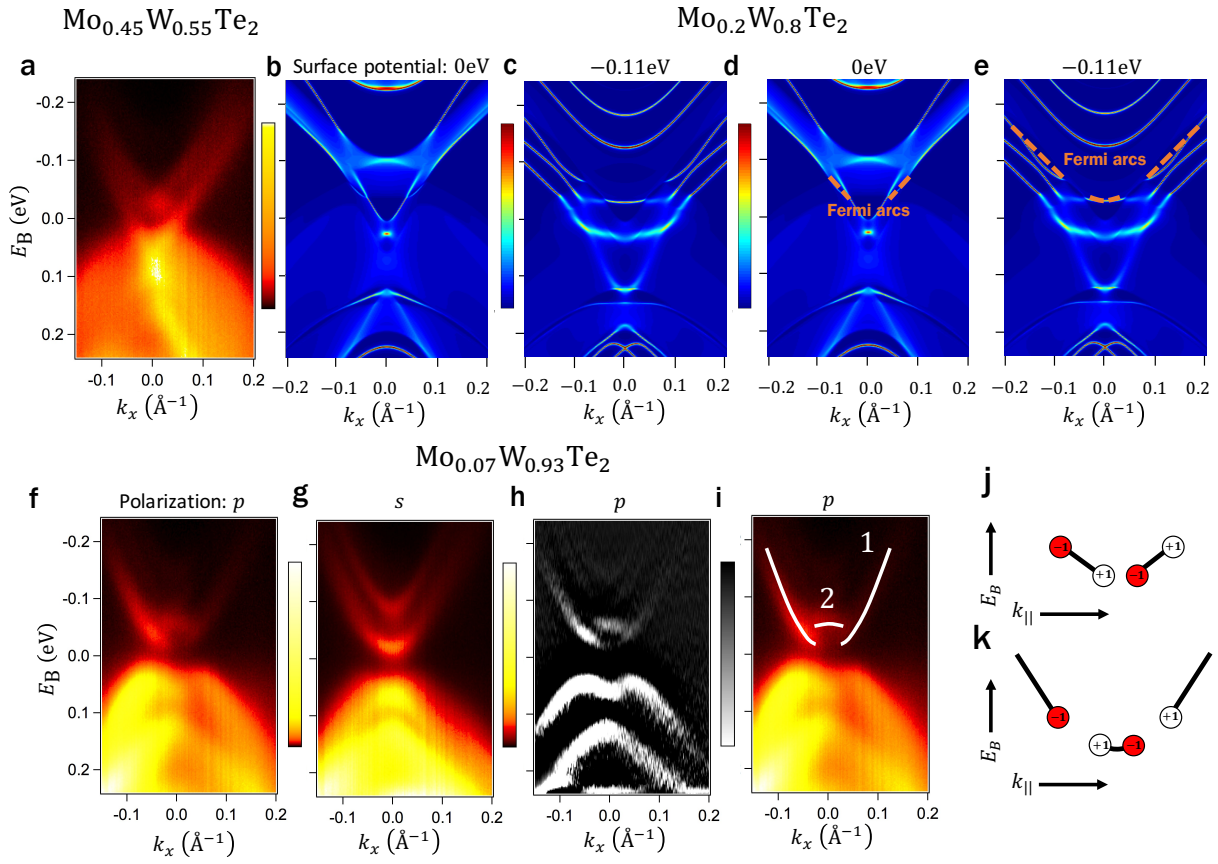
$Mo_{0.45}W_{0.55}Te_2$
$Mo_{0.2}W_{0.8}Te_2$
$Mo_{0.07}W_{0.93}Te_2$
a
b Surface potential: 0eV
c −0.11eV
d 0eV
e −0.11eV
Fermi arcs
Fermi arcs
f Polarization: p
g s
h p
i p
1
2
j
k
E_B (eV)
k_x (Å^{-1})
E_B
$k_{||}$

FIG. 4: **Signatures of Fermi arcs in $\mathbf{Mo_xW_{1-x}Te_2}$.** **a,** Pump-probe ARPES spectrum at $k_y = 0.325\text{Å}^{-1}$, showing disjoint features, as marked in Fig. 3 (g). **b,** *Ab initio* calculation at $k_y = k_{\text{W1}} = 0.215\text{Å}^{-1}$ with 0eV surface potential, showing trivial surface states which merge into the bulk bands, forming trivial arcs. The trivial disjoint features match the data well. **c,** Same calculation but with -0.11eV surface potential, showing topological Fermi arcs which match the data well. **d, e,** Same as (b, c) but with the arc marked by dotted orange lines. Note the many trivial surface states, many of which merge into the bulk, forming trivial arcs. The proliferation of trivial surface states complicates interpretation of the ARPES spectra. **f,** Pump-probe ARPES spectrum of $Mo_{0.07}W_{0.93}Te_2$ at $k_y = 0.29\text{Å}^{-1}$ and polarization p, emphasizing the disjoint feature and **g,** polarization s, showing two trivial electron surface states. Like $Mo_{0.45}W_{0.55}Te_2$, we the disjoint features consist of an inner arc and two outer arcs, as shown in **h,** a second derivative plot and **i,** marked on the data. Note that the inner arc is above the ends of the outer arcs in $Mo_{0.07}W_{0.93}Te_2$, while the inner arc is below the outer arcs in $Mo_{0.45}W_{0.55}Te_2$. This composition dependence suggests one route to clarifying whether or not we observe topological Fermi arcs. **j,** The connectivity of Fermi arcs we find with surface potential 0eV, with a W_1 connected to a W_2 and **k,** the connectivity for -0.11eV, with the two W_1 connected and two W_2 connected. This second scenario is suggested by our data.